Article:
Siampour, H., Wang, O., Zenin, V.A. et al. (10 more authors) (2020) Ultrabright single-photon emission from germanium-vacancy zero-phonon lines: deterministic emitter-waveguide interfacing at plasmonic hot spots. Nanophotonics, 9 (4). 36. pp. 953-962.

https://doi.org/10.1515/nanoph-2020-0036

Research article

Hamidreza Siampour*, Ou Wang, Vladimir A. Zenin, Sergejs Boroviks, Petr Siyushev, Yuanqing Yang, Valery A. Davydov, Liudmila F. Kulikova, Viatcheslav N. Agafonov, Alexander Kubanek, N. Asger Mortensen, Fedor Jelezko and Sergey I. Bozhevolnyi

Ultrabright single-photon emission from germanium-vacancy zero-phonon lines: deterministic emitter-waveguide interfacing at plasmonic hot spots

https://doi.org/10.1515/nanoph-2020-0036
Received January 16, 2020; revised February 28, 2020; accepted March 13, 2020

Abstract: Striving for nanometer-sized solid-state single-photon sources, we investigate atom-like quantum emitters based on single germanium-vacancy (GeV) centers isolated in crystalline nanodiamonds (NDs). Cryogenic characterization indicated symmetry-protected and bright (>10^6 counts/s with off-resonance excitation) zero-phonon optical transitions with up to 6-fold enhancement in energy splitting of their ground states as compared to that found for GeV centers in bulk diamonds (i.e. up to 870 GHz in highly strained NDs vs. 150 GHz in bulk). Utilizing lithographic alignment techniques, we demonstrate an integrated nanophotonic platform for deterministic interfacing plasmonic waveguides with isolated GeV centers in NDs, which enables 10-fold enhancement of single-photon decay rates along with the emission direction control by judiciously designing and positioning a Bragg reflector. This approach allows one to realize the unidirectional emission from single-photon dipolar sources, thereby opening new perspectives for the realization of quantum optical integrated circuits.

Keywords: unidirectional surface plasmon polariton (SPP) coupler; nanodiamonds; germanium-vacancy (GeV) centers; near-field microscopy; integrated quantum photonics.

1 Introduction

Efficient interfaces between single atoms and single photons are essential ingredients for building quantum optical networks, where atomic nodes (quantum emitters) are linking together via flying photons (qubits) [1, 2]. The key challenge here is to engineer atom-photon interactions in order to have control over individual quantum emitters on a large scale. Combining isolated atoms with nanophotonic systems is a powerful approach to strongly enhance the atom-photon interaction due to a large cooperativity associated with nanoscale photonic devices, although trapping atoms in tightly focused laser beams (optical tweezers) imposes serious technical challenges [3–5]. Alternatively, an all solid-state approach has been developed, in which naturally trapped "atoms" (e.g. quantum dots) are coupled, created, and multiplexed on a single chip [6]. Despite the progress made for deterministic positioning of quantum dots on a single chip [7–10], some challenges remain due to a relatively short coherence time available with quantum dots (in nanosecond range) [11], resulting in the quantum information being typically lost before reaching distant quantum nodes.

***Corresponding author: Hamidreza Siampour,** Centre for Nano Optics, University of Southern Denmark, Campusvej 55, Odense M, DK-5230, Denmark; and Department of Physics and Astronomy, University of Sheffield, Sheffield S3 7RH, United Kingdom, e-mail: h.siampour@sheffield.ac.uk. https://orcid.org/0000-0001-8476-0207
Ou Wang, Petr Siyushev, Fedor Jelezko: Institute for Quantum Optics, Ulm University, Albert-Einstein-Allee 11, D-89081 Ulm, Germany
Vladimir A. Zenin, Sergejs Boroviks and Alexander Kubanek: Centre for Nano Optics, University of Southern Denmark, Campusvej 55, Odense M, DK-5230, Denmark
Yuanqing Yang: Centre for Nano Optics, University of Southern Denmark, Campusvej 55, Odense M, DK-5230, Denmark; and Advanced Semiconductor Materials Lithography (ASML), 5504DR Veldhoven, Netherlands. https://orcid.org/0000-0001-7139-1254
Valery A. Davydov and Liudmila F. Kulikova: L.F. Vereshchagin Institute for High Pressure Physics, Russian Academy of Sciences, Moscow 108840, Russia
Viatcheslav N. Agafonov: GREMAN, UMR CNRS CEA 6157, Université de Tours, 37200 Tours, France
N. Asger Mortensen and Sergey I. Bozhevolnyi: Centre for Nano Optics, University of Southern Denmark, Campusvej 55, Odense M, DK-5230, Denmark; and Danish Institute for Advanced Study, University of Southern Denmark, Campusvej 55, Odense M, DK-5230, Denmark

Further search for configurations ensuring long coherence times in atomic systems and allowing for scalable implementation in solid-state systems led to the exploration of diamond crystals containing artificial "atoms" (so-called color centers) [12]. Starting with a nitrogen-vacancy (NV) center (i.e. substitutional nitrogen-atom impurity next to a diamond lattice vacant site), remarkable coherence time (in millisecond range) [13] has been achieved, making it an ideal emitter for spin physics and metrology [14]. However, a lack of symmetry in NV molecular structure severely limits the coherent part of the emission, with the emission to a zero-phonon line (ZPL) being only 4%, and makes the frequency of optical transitions very sensitive to the environment. Replacing nitrogen with larger atoms of group IV in the periodic table (e.g. with a silicon atom that is ~1.5 times larger in size than a carbon atom) enabled circumventing the issues associated with symmetry arguments [15–20] (see Figure 1A). The defect atom in group IV (silicon, germanium, tin, or lead) is placed between two diamond lattice vacant sites, resulting in a split-vacancy color center [silicon vacancy (SiV), germanium vacancy (GeV), tin vacancy (SnV), or lead vacancy (PbV)] with spectral stability as a result of its inversion symmetry. This opened a way toward demonstrations of indistinguishable solid-state quantum emitters (without the need for electric field tuning) with spectral stability and large ZPLs

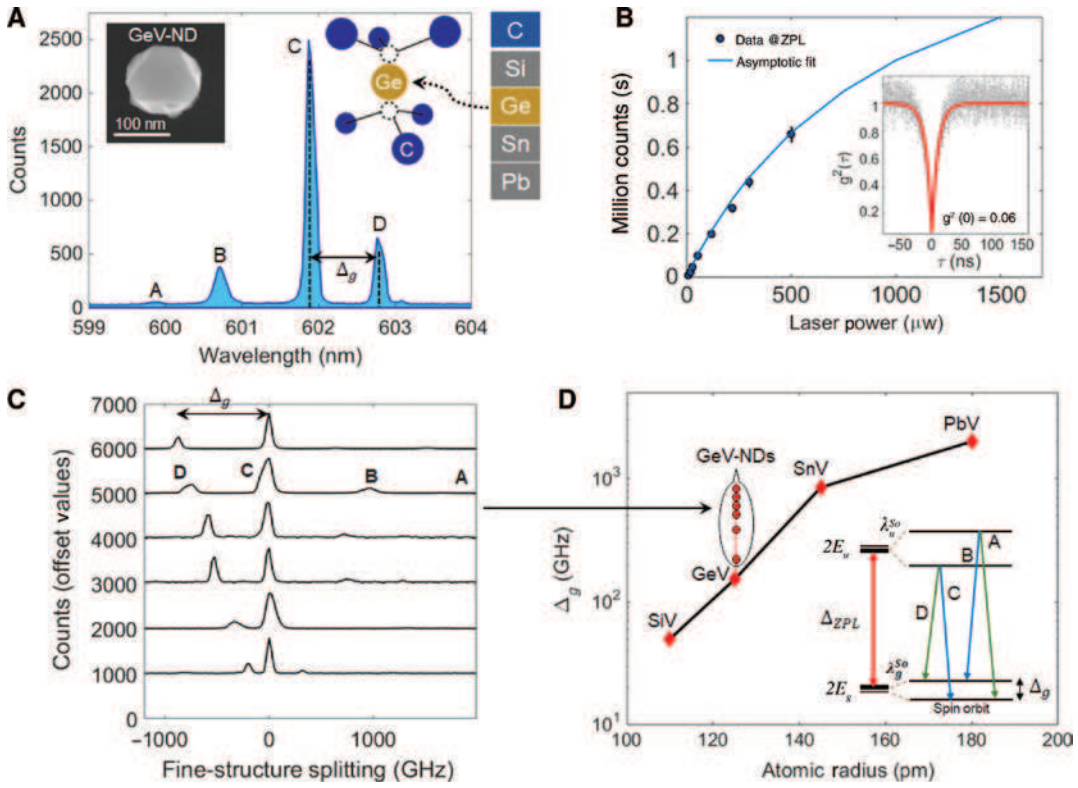

Figure 1: Color centers in diamond crystals with structural symmetries and bright ZPLs.
(A, B) Characterization of a single GeV center in an HPHT ND. Spectrum taken at a cryogenic temperature exhibits a four-line fine structure at around 602 nm similar to bulk crystals (A). Inset shows an SEM image of the ND. The temperature of the ND was calculated to be ~40 K using Boltzmann statistics [21], which is higher than the temperature of the cryostat cold finger due to the limited thermal conductivity of the substrate (silicon). (B) Power dependency measurements indicates ultrabright ZPLs (exceeding 1 million counts/s at 1 mW). The saturation curve was fitted to an asymptotic function [$I = I_\infty \cdot P/(P+P_\infty)$, where I_∞ and P_∞ are saturated intensity and saturated power, respectively], indicating a 15-fold enhancement in brightness compared to those reported for bulk diamonds [22]. Inset shows a strong antibunching dip in autocorrelation measurement [$g^2(0) = 0.06$], which implies single photon emission. The red line represents a single exponential fit [16]. (C, D) Energy splitting in the ground states (Δ_g) for different GeV-ND samples were measured and shown in (C) and compared with other group IV color centers in diamond (D). (D) The larger atom exhibits larger splitting and a potentially longer spin coherence time. The values of Δ_g for color centers in bulk diamond, including SiV [19], GeV [16], SnV [17], and PbV [18], were adapted from the experimental results reported for the corresponding vacancies. Having GeV centers in NDs results in even larger energy splitting in the ground state [up to 870 GHz as shown in (C)] due to the strain conditions in nanocrystals. Inset shows zero-phonon optical transition lines for a typical group IV color center. Internal transitions of B and C are parallel in polarization and orthogonal to the external transitions of A and D, resulting in an emitter with two orthogonal dipoles [19, 23].

[24]. However, the efficiency of photon outcoupling from diamond color centers in bulk crystals is limited (due to a high refractive index of diamond), as mentioned before in Refs. [12, 16, 17, 23, 25–29].

Progressing toward bright and efficient nanometer-sized solid-state single-photon sources, we here report on the first characterization of individual GeVs in nanodiamonds (NDs) at low temperatures, allowing us to resolve four zero-phonon transitions and actually characterize the ground-level splitting (unlike our previous work at room temperature [30] and other low-temperature results with GeV in bulk diamonds [16, 22, 31]). Additionally, this is the first demonstration that the dielectric-loaded surface plasmon polariton waveguide (DLSPPW) platform survives cooling to low temperatures, which is not trivial at all because of the different materials in this platform. The usage of gold crystals was also dictated by the necessity to conduct low-temperature experiments taking a much longer time. Cryogenic characterization indicated symmetry-protected and bright (>10^6 counts/s with off-resonance excitation) zero-phonon optical transitions featuring remarkable energy splitting in their ground states, up to 870 GHz, which is ~6 times larger than that in bulk diamonds. The large energy splitting in the ground state implies a potentially longer spin coherence due to the suppressed phonon-mediated transitions between the lower and upper branches [17, 32]. This opens new perspectives for deterministic interfacing of isolated atoms with photons along with merging quantum emitters with highly confined surface plasmons in metal-based nanostructures [5, 33–35]. Utilizing lithographic alignment techniques [30, 34, 36, 37], we demonstrate an integrated nanophotonic platform for deterministic interfacing plasmonic waveguides with isolated GeV centers in NDs, which enables 10-fold enhancement of single-photon decay rates along with the emission direction control by judiciously designing and positioning a Bragg reflector. This approach allows one to realize the unidirectional emission from single-photon dipolar sources, thereby opening new perspectives for integrated quantum nanophotonics.

2 Results and discussion

Imitating the natural formation of diamonds underneath the earth, diamond crystals were grown at the nanometer scale, under a high-pressure high-temperature (HPHT) condition, and Ge defect atoms were added during the growth in a hydrocarbon metal catalyst-free system based on homogeneous mixtures of naphthalene $C_{10}H_8$ with tetraphenyl germanium $C_{24}H_{20}Ge$ (see details in Supplementary Section 1). Cryogenic characterization shows symmetry-protected optical transitions for the synthesized GeV centers in NDs (see Figure 1A, C), following the reported trend for bulk diamonds [16–19]. Furthermore, ZPLs indicate a large splitting in the ground state (up to 870 GHz), which is ~17 times larger than SiV [19] and ~6 times larger than GeV in bulk [16, 22, 31], becoming close to SnV with 850 GHz [17] (see Figure 1D). It has already been demonstrated that the strain environment can mitigate the effect of thermal phonon bath on a diamond spin qubit and eventually suppress phonon-induced decoherence without lowering the operating temperature [38]. Our results for GeV centers represent the first step in this direction, showing a significant enhancement in the ground-state splitting under the inherently forced tensile strain in NDs. The results can open the way toward further investigation, e.g. use of a nano-electro-mechanical system device [38], in order to have higher control over the strain conditions and thereby allow for engineering of electron-phonon interaction in GeV centers. Power dependency measurements at low temperatures (shown in Figure 1B) exhibit ultrabright single-photon count rates (~2×10^6 counts/s, an approximated value at saturation) at ZPLs (i.e. excluding phonon sideband) with clean single-photon emission [strong antibunching dip of $g^2(0) = 0.06$, where $g^2(0)$ is the autocorrelation function at zero-delay time]. Compared with the brightness of GeV in bulk diamond reported by Iwasaki et al. [22], a significant (15-fold) enhancement in the brightness is achieved, from 170,000 counts/s in bulk to 2 million counts/s in ND. This increase can be attributed to the circumstances that nanometer-sized NDs would not suffer from the emission loss due to the total internal reflection at diamond-air interfaces and that the Purcell enhancement from GeV emitters coupling to SPPs supported by the air-gold interface further increases their brightness. The measurements performed for another GeV-ND, resulting in 1.3 million counts/s for 1000 μW laser power (see Supplementary Figure 19S), are consistent in the saturation with the measurements shown in Figure 1B. Deterministic loading of dielectric nanostructures on colloidal gold crystals enabled trapping a preselected ND at a plasmonic hot spot for realizing a sustainable nanoplasmonic platform for integrated quantum photonics. This introduces a powerful approach, alternative to the current deterministic techniques – atomic force microscope (AFM) manipulation [39], site-controlled and strain-induced excitation [8], in situ cathodoluminescence lithography [9], and optical trapping [3, 5] – to improve the level of control on coupling and, at the same time, to facilitate scalable fabrication (see Figure 2).

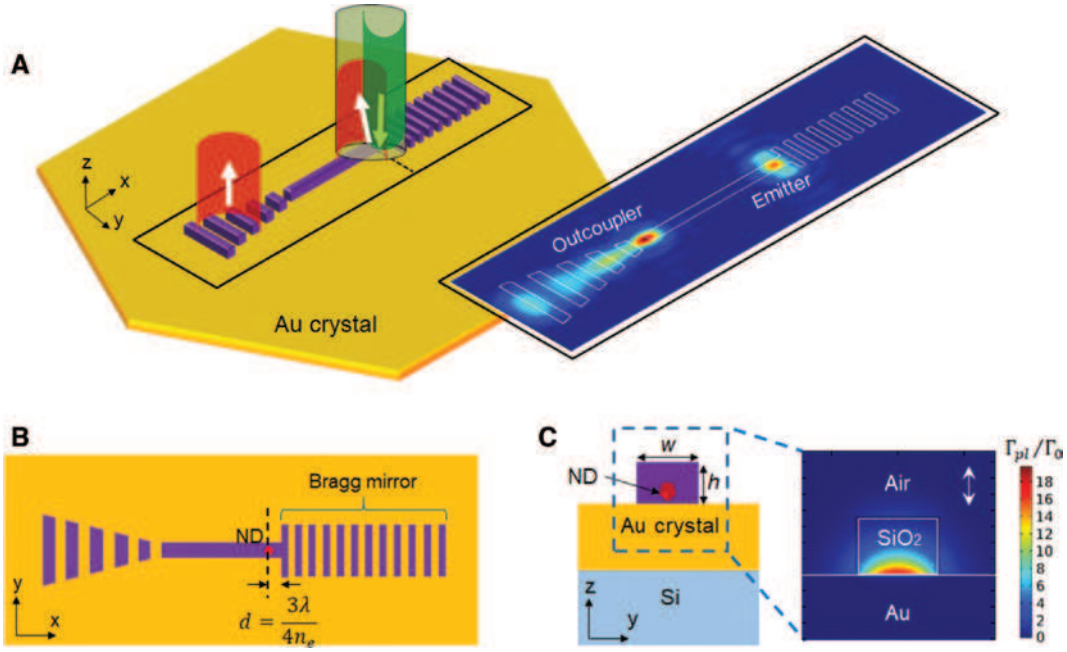

Figure 2: Deterministic emitter-waveguide interface for highly directional light emission.
(A, B) Schematic of the device layout and working principle. Using optical positioning of bright centers in NDs and electron beam lithographic alignment, dielectric nanoridges were fabricated atop gold crystals, so that the preselected ND is embedded in the nanoridge and positioned in the second constructive interference fringe of the RBG mirror (A, B). Simulated far-field image for the coupled system (A, right). (C) Mode profile indicates distribution of Purcell enhancement (Γ_{pl}/Γ_0, plasmonic decay rate) for the GeV coupled system, while $w = 250$ nm and $h = 180$ nm.

In the experiment, colloidal gold crystals were grown on a silicon substrate using a thermolysis synthesis technique [40] (see details in Supplementary Section 2). Lithographic alignment markers were made on top of (and nearby) the gold crystals, and NDs were deposited on the substrate afterwards. The sample was then loaded on the cold finger of a continuous-flow helium cryostat, which was cooled to 4.7 K for confocal microscopy measurements (see Section 4.2). A fluorescence image was taken from a crystalline gold flake on which NDs containing single GeV centers were deposited (see Supplementary Figure 4S for the corresponding confocal image). A single GeV emitter was selected based on fluorescence spectrum measurements, and its location was determined with respect to the markers. Utilizing lithographic alignment techniques [30, 34, 36, 37], we fabricated a waveguide-mirror configuration with reflecting Bragg gratings (RBGs), where the preselected ND is embedded in the waveguide. Realization of the unidirectional coupler requires implementing the waveguide-emitter coupling exactly at the specific constructive interference point (at the distance of the second constructive point of the RBG mirror, i.e. $d = 3\lambda_n/4$, where λ_n is the wavelength of the plasmonic mode [41]), as shown in Figure 2A and B. This means that a higher degree of accuracy is needed for the deterministic realization of the device. Without such determination, the emitter may be placed at the destructive interference points ($d = i\lambda/2n_e$, $i = 1, 2, \ldots, n$) for which the emission rate is becoming suppressed by a factor of $(1 - R)^2$, instead of being empowered by $(1 + R)^2$, where R represents the reflectance of the RBG mirror (see Supplementary Figure 18S).

A scanning electron microscopy (SEM) image of the fabricated device is shown in Figure 3A. Excited with the green laser ($\lambda = 532$ nm), the fluorescence light was collected from the excitation point (GeV-ND) and away of it within several micrometers using a galvanometric scanning mirror. The result is illustrated in Figure 3B, showing two spots, one from the excited GeV emitter and the other from the grating output at the end (outcoupler). This indicated coupling of GeV emission to the waveguide mode (DLSPPW mode) of the unidirectional SPP device. Plasmonic decay (Γ_{pl}/Γ_0) of GeV emission to the fundamental transverse magnetic (TM) mode of the DLSPPW is maximized for the emission transition dipole moment oriented perpendicular to the gold plane (z-axis), as shown in the simulation results in Supplementary Figure 16S. The results indicate that ~85% of the plasmonic decay is due to the coupling of this transverse out-of-plane dipole to the DLSPPW mode [Figure 16S(b)-left]. There is also an ~14% contribution from the longitudinal dipole oriented along the waveguide axis, i.e. along the x-axis [Supplementary Figure 16S(c)-left], while there is almost no contribution

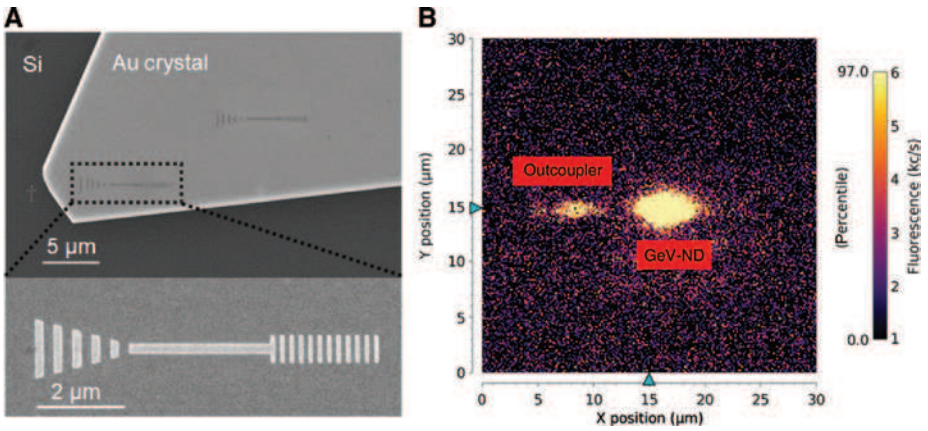

Figure 3: Unidirectional plasmonic excitation of a single GeV color center in an ND.
(A) SEM image of the fabricated device on gold crystal. The periodicity of the RBG is 240 nm. (B) Galvanometric mirror scan image of the coupled system.

from the transverse in-plane, i.e. along the *y*-axis, dipole [Supplementary Figure 16S(d)-left]. These differences are dictated by the DLSPPW mode polarization content [42, 43], so that the main DLSPPW mode power contribution originates from the emission dipole component, which is perpendicular to the sample surface (i.e. the projection of the dipole source on the *z*-axis). To compare with the experimental observations, we implemented the far-field projection to simulate the far-field images observed by a microscope with 0.95 numerical aperture (NA) (as discussed in Section 4.4). The results indicate that the electric dipole source that is oriented along the *z*-axis [see Supplementary Figure 16S(b)-right], i.e. the transverse out-of-plane dipole, is the one that is the strongest coupled to the fundamental DLSPPW mode (because the transverse out-of-plane electric field component of the fundamental DLSPPW mode is the strongest one), producing a visible spot at the outcoupling grating, while the contributions of other two dipoles are negligible [no outcoupled spots are seen in Supplementary Figure 16S(c,d)-right]. In the simulations, for each dipole source with a specific polarization component, we plot all polarization components of the generated far-field distributions.

Fluorescence spectra taken from the embedded GeV-ND at the center and from the output grating at the waveguide end are shown in Figure 4A and B, respectively. For this ND, all four ZPLs have been merged together and appeared as a single line at 605 nm. The merging of the ZPLs observed in this experiment (Figure 4) is not really understood; however, the stability of the line for elevated temperatures (shown in Supplementary Figure 7S) and the room-temperature measurements (with no bleaching or blinking) confirm that the observed emission line should indeed be ascribed to an individual GeV center in this particular ND. The ZPL shift, from 602 to 605 nm, in this sample can be explained by the occurrence of the isotopic substitution of the impurity atom and specific isotopic compression of the carbon lattice, as discussed in Ref. [44]. These isotopic shifts of the ZPLs have also been reported for SiV centers (see, e.g. Ref. [45]). Lifetime measurements before and after structure fabrication indicate a 5-fold lifetime shortening from 11.2 ns (Figure 4C, ND on gold flake) to 2.3 ns (Figure 4D, ND embedded in device). The lifetime data were analyzed by a single exponential fit with a fast decay within the first few nanoseconds of the data being excluded in the fitting, as these are related to background fluorescence. Considering an additional 2-fold lifetime reduction due to the metal layer [30] (see Supplementary Section 11), we estimated a 10-fold enhancement in the total decay rate of the GeV emitter, a remarkable record due to the interaction with the unidirectional SPP coupler (see Supplementary Figure 5S–11S for further details and additional experiments). Furthermore, we demonstrated another experiment with a single NV center for which the periodicity of the RBG was tuned for NV ZPL (637nm), and we see a 6-fold lifetime shortening (from 26.3 to 4.3) for the coupled NV, as shown in Supplementary Figure 8S(i), indicating a 12-fold decay rate enhancement in total (due to the additional 2-fold reduction for the metal layer).

In order to verify the properties of the unidirectional SPP coupler, we performed scanning near-field optical microscopy (SNOM) measurements with a titanium sapphire laser source (wavelength 775–1000 nm). To experimentally evaluate the reflectance of the RBGs, the periodicity of the Bragg grating was scaled up from 240 nm (designed for the GeV ZPL) to 380 nm (designed for $\lambda = 850$ nm) in order to increase the central Bragg wavelength to those available in our SNOM setup. Because

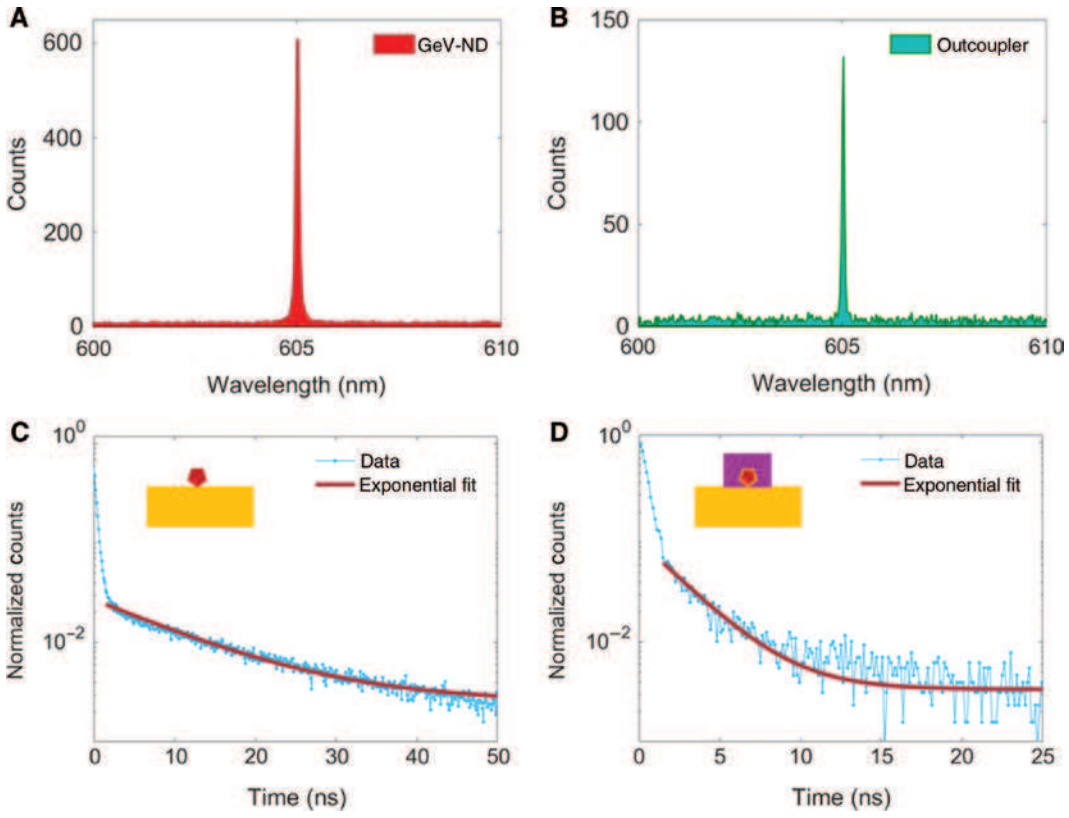

Figure 4: Characterization of a GeV-ND coupled to the unidirectional SPP waveguide device.
(A, B) Spectra taken from the embedded GeV-ND (A) and from the outcoupled light at the end (B). (C, D) Lifetime measurement data from uncoupled GeV (C; ND on gold crystal), and coupled GeV (D; ND embedded in the device). The data were analyzed with a single exponential function [$I_{tot} = A \cdot \exp(-t/\tau_A) + C$, where τ_A indicates the lifetime, and A and C are constants] [16, 30], indicating a 5-fold lifetime shortening from 11.2 ns (ND on gold flake) to 2.3 ns (ND embedded in device). Considering an additional 2-fold reduction due to the metal layer [30], we estimated a 10-fold decay rate enhancement in total (see Supplementary Section 11).

our SNOM is operating in a transmission configuration with sample illuminated from below, a grating was fabricated in the gold layer for efficient excitation of plasmonic mode (see schematic in Figure 5A and details in Section 4). An SEM image of the fabricated device and an AFM image of the excitation point are shown in Figure 5B and C, respectively. The RBG mirror period was modified to produce strong back-reflection at the central operating wavelength (Figure 5D, $\lambda = 850$ nm), while no reflection was observed outside the TM bandgap (Figure 5E, $\lambda = 1000$ nm). Mode parameters (effective mode index, propagation length, and reflection coefficient) were extracted from near-field maps, obtained for different laser wavelengths, using a simple fitting procedure [46–48] (see Supplementary Figures 13S and 14S). The resulting SNOM measurements indicate ~80% reflectance from the RBG mirror (Figure 5G).

Adding a Bragg reflector to the end of the waveguide has a great potential to enhance the Purcell factor further up to $(1+R)^2$ times (in addition to the enhancement associated with the plasmonic waveguide itself), where R denotes the reflectivity. For the Bragg reflector with 80% reflectivity (as measured in our near-field setup) and the emitter located at the constructive interference node, one can estimate an ~3.25 times Purcell enhancement in addition to the enhancement achieved due to the plasmonic waveguide system (see Supplementary Figure 18S). As mentioned already in the article, the main advantage of GeV centers (and in general group IV color centers) is their structural symmetries leading to indistinguishability of photons emitted from different emitters. Our cryogenic measurements clearly show that the zero-phonon optical transitions for the synthesized GeV centers in NDs are indeed protected by inversion symmetry (see four-line fine structure in Figure 1A) and therefore have a great potential to create indistinguishable or "coherent" photons. Furthermore, our achievement in Purcell enhancement by using a deterministic emitter-waveguide interface at plasmonic hot spots (constructive nodes) of the Bragg reflector is one of the important steps needed for realizing the plasmonic speed-up strategy for overcoming quantum decoherence. The plasmonic speed-up approach is a

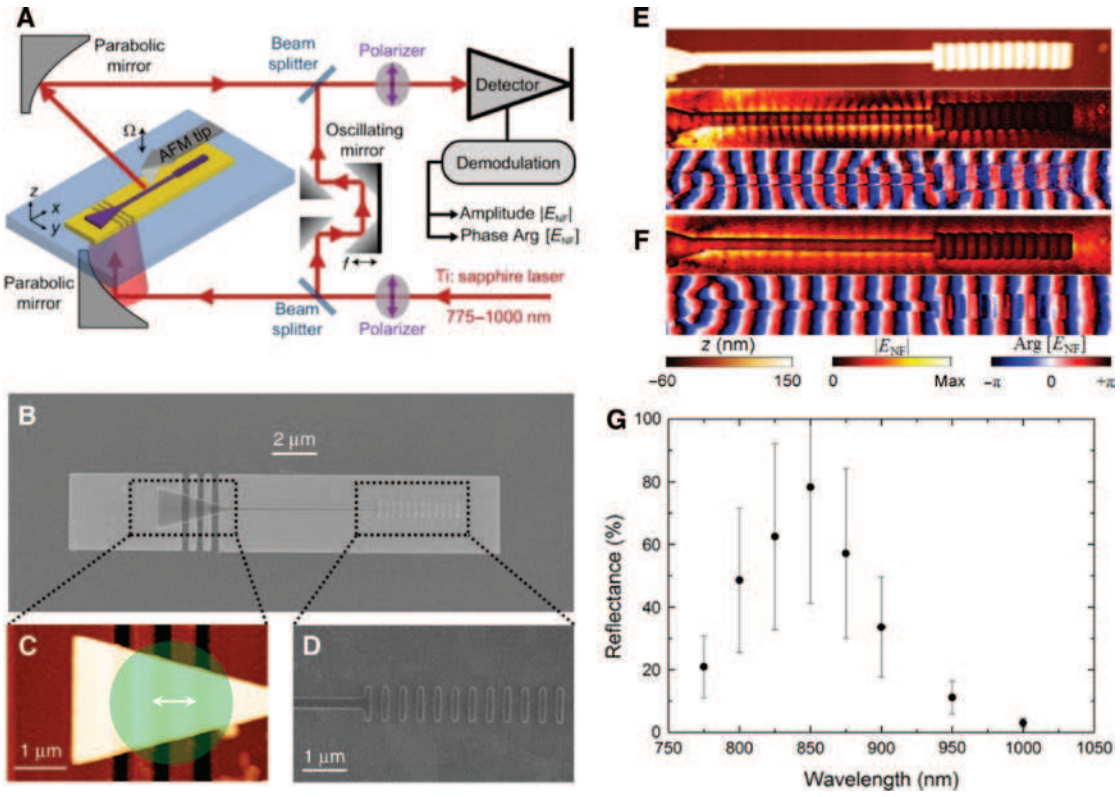

Figure 5: Near-field investigation of the unidirectional SPP coupler.
(A) Schematic of the near-field optical setup. (B) SEM image of the fabricated device, namely dielectric nanoridge atop a patterned gold rectangular layer. (C) AFM image of the input grating, overlapped with dielectric funnel for excitation of dielectric-loaded SPP mode. Green circle and white arrow illustrate the approximate position of incident illumination spot (not to scale) and its polarization, respectively. (D) Zoomed-in SEM image of RBG. (E, F) Topography z (top), near-field amplitude $|E_{NF}|$ (middle), and phase Arg $[E_{NF}]$ (bottom) of the unidirectional SPP coupler, recorded at $\lambda = 850$ nm (E, inside the TM bandgap) and $\lambda = 1000$ nm (F, outside the TM bandgap). (G) Reflectance of RBG, evaluated from SNOM maps.

new technology trend aiming to enhance the light-matter interaction and thereby shorten the spontaneous emission time in quantum emitters, so that it would eventually outpace fast quantum decoherence rates in matter and beat the dephasing time (see, e.g. the recent perspective paper by Bogdanov et al. published in *Science* [49]).

3 Conclusions

GeV centers in diamond nanocrystals have been investigated at low temperatures, indicating symmetry-protected and ultrabright (2×10^6 counts/s, an approximated value at saturation) zero-phonon optical emission. A large energy splitting of 870 GHz in the ground state has been determined for the GeV centers in highly strained ND samples, which is ~6 times larger than that in bulk diamonds. An integrated crystalline gold-based nanophotonic platform has been realized, on which optical centers in NDs interface with highly confined SPP modes in a unidirectional manner, resulting in remarkable Purcell enhancements (10-fold enhancement for GeV-ND and 12-fold for NV-ND). The unidirectional interaction enables efficient guiding control of the emitted single photons, revealing the potential of our approach for realizing on-chip quantum optical network.

4 Methods

4.1 Device fabrication

Direct e-beam writing was performed using a negative-tone electron-beam resist composed of 6% solution of hydrogen silsesquioxane (HSQ) diluted in methyl isobutyl ketone solvent [XR-1541-006 (6%), Dow Corning, MI, USA]. Using a standard spin-on coating equipment, HSQ was deposited

on the substrate at a speed of 1200 rpm (1 min), and subsequently the solvent was boiled off during a hotplate bake process (170°C, 2 min). This resulted in a 180-nm film on gold crystal flakes. Using a single exposure tool with 30-keV beam energy and area doses from 400 to 700 μC/cm^2, the HSQ film was patterned, with capability to define features as small as 6 nm, and nanoridge waveguides were defined and accurately positioned onto preselected NDs, whose locations were determined with respect to the specifically designed and prefabricated alignment markers. Then, the HSQ film was developed in tetramethylammonium hydroxide (25 wt.% solution in water, Sigma-Aldrich, MO, USA), a standard aqueous base developer (see further details in Supplementary Figure 5S). After the development, HSQ turned to silicon dioxide (SiO_2).

4.2 Cryogenic measurements

The sample was mounted on the cold finger of a continuous-flow helium cryostat, which was cooled to 4.7 K for imaging with a home-built confocal microscope (see details in Supplementary Figure 3S). Experimental control was provided by the Qudi software suite [50]. The GeV centers were off-resonantly excited by linearly polarized 532-nm green laser to map the fluorescence of GeV ZPL. A band-pass filter (599/13 nm) was placed in front of the avalanche photodiode. Spectra were measured after a 560-nm long-pass filter (Supplementary Figure 3S).

4.3 SNOM

Near-field investigation was performed using commercial AFM-based scattering-type SNOM (NeaSpec, Munich, Germany). In this setup, used in transmission mode, the sample was illuminated normally from below (focused by a bottom parabolic mirror with NA ~0.3) using a tunable continuous-wave Ti:sapphire laser (wavelength 775–1000 nm, Spectra Physics, MA, USA). The illumination was coupled into the waveguiding SPP mode by means of a grating in the gold layer. The sample was scanned in a non-contact mode by a commercial Pt-coated AFM tip (Arrow-NCPt from NanoWorld, Neuchâtel, Switzerland), which acts as a scatterer of the near field. The tapping amplitude and frequency were ~60 nm and Ω ~250 kHz, correspondingly. The tip's scattered light was collected by a top parabolic mirror (NA ~0.7) and forwarded toward a photodetector. In order to resolve both amplitude and phase, a Mach-Zehnder interferometer was integrated into our setup, in which the optical path difference was modulated by an oscillating mirror in the reference arm (frequency f ~300 Hz). The detected signal was then demodulated using a pseudo-heterodyne detection method [51] (see further details in Supplementary Figure 12S–14S).

4.4 Numerical simulations

Finite-difference time-domain (FDTD) simulations were performed using a commercial software (FDTD Solutions v8.11.318, Lumerical, Vancouver, BC, Canada). Perfectly matched layers were applied to enclose the computational domain of 8.5 μm × 3 μm × 2 μm in all calculations. The finest mesh grid size of 5 nm was used in the simulations. The optical constants of the gold were taken from the experimental data reported by Johnson and Christy [52]. To mimic the experimental conditions, we utilized an electric dipole oriented along different directions to excite the propagating mode in the waveguide. The distance between the dipole and the RBG mirror was set as $d = 3\lambda_n/4$ for an efficient unidirectional excitation while the height of the dipole was set to 30 nm. To compare with the experimental observations, we implemented far-field projection to simulate the far-field images observed by a microscope with NA 0.95 [53] (see Supplementary Figure 16S). We added further simulations in order to mimic the experimental conditions at cryogenic temperatures. Cooling to cryogenic temperatures allows one to suppress the SPP propagation losses due to the reduction in the collision frequency of free electrons, as discussed in Supplementary Section 14.

Acknowledgments: This work was supported by the European Research Council (ERC), Advanced Grant 341054, Funder Id: http://dx.doi.org/10.13039/100010663 (PLAQNAP). FJ acknowledges support of the DFG, BMBF, VW Stiftung, and EU (ERC, DIADEMS). VAZ, SB, and NAM acknowledges support of VILLUM FONDEN (grant no. 16498). VAD and LFK thank the Russian Foundation for Basic Research (grant no. 18-03-00936) for financial support. AK acknowledges support of the DFG, the Carl-Zeiss Foundation, IQST, and the Wissenschater-Ruckkehrprogramm GSO/GZS.

References

[1] Humphreys PC, Kalb N, Morits JPJ, et al. Deterministic delivery of remote entanglement on a quantum network. Nature 2018;558:268–73.

[2] Wehner S, Elkouss D, Hanson R. Quantum internet: a vision for the road ahead. Science 2018;362:eaam9288.

[3] Thompson JD, Tiecke TG, de Leon NP, et al. Coupling a single trapped atom to a nanoscale optical cavity. Science 2013;340:1202.
[4] Gullans M, Tiecke TG, Chang DE, et al. Nanoplasmonic lattices for ultracold atoms. Phys Rev Lett 2012;109:235309.
[5] Tiecke TG, Thompson JD, de Leon NP, Liu LR, Vuletić V, Lukin MD. Nanophotonic quantum phase switch with a single atom. Nature 2014;508:241.
[6] Lodahl P, Floris van Driel A, Nikolaev IS, et al. Controlling the dynamics of spontaneous emission from quantum dots by photonic crystals. Nature 2004;430:654.
[7] Badolato A. Deterministic coupling of single quantum dots to single nanocavity modes. Science 2005;308:1158–61.
[8] Luo Y, Shepard GD, Ardelean JV, et al. Deterministic coupling of site-controlled quantum emitters in monolayer WSe_2 to plasmonic nanocavities. Nat Nanotechnol 2018;13:1137–42.
[9] Schnauber P, Schall J, Bounouar S, et al. Deterministic integration of quantum dots into on-chip multimode interference beamsplitters using in situ electron beam lithography. Nano Lett 2018;18:2336–42.
[10] Akimov AV, Mukherjee A, Yu CL, et al. Generation of single optical plasmons in metallic nanowires coupled to quantum dots. Nature 2007;450:402–6.
[11] Thorgrimsson B, Kim D, Yang Y-C, et al. Extending the coherence of a quantum dot hybrid qubit. NPJ Quant Inform 2017;3:32.
[12] Sipahigil A, Evans RE, Sukachev DD, et al. An integrated diamond nanophotonics platform for quantum-optical networks. Science 2016;354:847–50.
[13] Balasubramanian G, Neumann P, Twitchen D, et al. Ultralong spin coherence time in isotopically engineered diamond. Nat Mater 2009;8:383.
[14] Doherty MW, Manson NB, Delaney P, Jelezko F, Wrachtrup J, Hollenberg LCL. The nitrogen-vacancy colour centre in diamond. Phys Rep 2013;528:1–45.
[15] Rogers LJ, Jahnke KD, Doherty MW, et al. Electronic structure of the negatively charged silicon-vacancy center in diamond. Phys Rev B 2014;89:235101.
[16] Bhaskar MK, Sukachev DD, Sipahigil A, et al. Quantum nonlinear optics with a germanium-vacancy color center in a nanoscale diamond waveguide. Phys Rev Lett 2017;118:223603.
[17] Iwasaki T, Pingault B, Wan NH, et al. Tin-vacancy quantum emitters in diamond. Phys Rev Lett 2017;119:253601.
[18] Trusheim ME, Wan NH, Chen KC, et al. Lead-related quantum emitters in diamond. Phys Rev B 2019;99:075430.
[19] Hepp C, Müller T, Waselowski V, et al. Electronic structure of the silicon vacancy color center in diamond. Phys Rev Lett 2014;112:036405.
[20] Ditalia Tchernij S, Lühmann T, Herzig T, et al. Single-photon emitters in lead-implanted single-crystal diamond. ACS Photon 2018;5:4864–71.
[21] Clark CD, Kanda H, Kiflawi I, Sittas G. Silicon defects in diamond. Phys Rev B 1995;51:16681–8.
[22] Iwasaki T, Regan B, Kianinia M, Bray K, Toth M, Aharonovich I. Germanium-vacancy single color centers in diamond. Sci Rep 2015;5:12882.
[23] Rogers LJ, Wang O, Liu Y, et al. Single SiV centers in low-strain nanodiamonds with bulklike spectral properties and nanomanipulation capabilities. Phys Rev Appl 2019;11:024073.
[24] Sipahigil A, Jahnke KD, Rogers LJ, et al. Indistinguishable photons from separated silicon-vacancy centers in diamond. Phys Rev Lett 2014;113:113602.
[25] Babinec TM, Hausmann BJM, Khan M, et al. A diamond nanowire single-photon source. Nat Nanotechnol 2010;5:195.
[26] Evans RE, Bhaskar M, Sukachev D, et al. Photon-mediated interactions between quantum emitters in a diamond nanocavity. Science 2018;362:662.
[27] Riedrich-Möller J, Kipfstuhl L, Hepp C, et al. One- and two-dimensional photonic crystal microcavities in single crystal diamond. Nat Nanotechnol 2012;7:69–74.
[28] Dory C, Vercruysse D, Yang KY, et al. Inverse-designed diamond photonics. Nat Commun 2019;10:3309.
[29] Englund D, Shields B, Rivoire K, et al. Deterministic coupling of a single nitrogen vacancy center to a photonic crystal cavity. Nano Lett 2010;10:3922–6.
[30] Siampour H, Kumar S, Davydov VA, Kulikova LF, Agafonov VN, Bozhevolnyi SI. On-chip excitation of single germanium vacancies in nanodiamonds embedded in plasmonic waveguides. Light Sci Appl 2018;7:61.
[31] Siyushev P, Metsch MH, Ijaz A, et al. Optical and microwave control of germanium-vacancy center spins in diamond. Phys Rev B 2017;96:081201.
[32] Jahnke KD, Sipahigil A, Binder JM, et al. Electron-phonon processes of the silicon-vacancy centre in diamond. N J Phys 2015;17:043011.
[33] de Leon NP, Shields BJ, Yu CL. Tailoring light-matter interaction with a nanoscale plasmon resonator. Phys Rev Lett 2012;108:226803.
[34] Siampour H, Kumar S, Bozhevolnyi SI. Chip-integrated plasmonic cavity-enhanced single nitrogen-vacancy center emission. Nanoscale 2017;9:17902–8.
[35] Fernández-Domínguez AI, Bozhevolnyi SI, Mortensen NA. Plasmon-enhanced generation of nonclassical light. ACS Photon 2018;5:3447–51.
[36] Sapienza L, Davanço M, Badolato A, Srinivasan K. Nanoscale optical positioning of single quantum dots for bright and pure single-photon emission. Nat Commun 2015;6:7833.
[37] Siampour H, Kumar S, Bozhevolnyi SI. Nanofabrication of plasmonic circuits containing single photon sources. ACS Photon 2017;4:1879–84.
[38] Sohn Y-I, Meesala S, Pingault B, et al. Controlling the coherence of a diamond spin qubit through its strain environment. Nat Commun 2018;9:2012.
[39] Bogdanov SI, Shalaginov MY, Lagutchev AS, et al. Ultrabright room-temperature sub-nanosecond emission from single nitrogen-vacancy centers coupled to nanopatch antennas. Nano Lett 2018;18:4837–44.
[40] Boroviks S, Wolff C, Linnet J, et al. Interference in edge-scattering from monocrystalline gold flakes [Invited]. Opt Mater Express 2018;8:3688–97.
[41] López-Tejeira F, Rodrigo SG, Martín-Moreno L, et al. Efficient unidirectional nanoslit couplers for surface plasmons. Nat Phys 2007;3:324.
[42] Han Z, Bozhevolnyi SI. Radiation guiding with surface plasmon polaritons. Rep Progr Phys 2013;76:016402.
[43] Fakonas JS, Lee H, Kelaita YA, Atwater HA. Two-plasmon quantum interference. Nat Photon 2014;8:317–20.
[44] Ekimov EA, Krivobok VS, Lyapin SG, Sherin PS, Gavva VS, Kondrin MV. Anharmonicity effects in impurity-vacancy centers

in diamond revealed by isotopic shifts and optical measurements. Phys Rev B 2017;95:094113.
[45] Dietrich A, Jahnke KD, Binder JM, et al. Isotopically varying spectral features of silicon-vacancy in diamond. N J Phys 2014;16:113019.
[46] Andryieuski A, Zenin VA, Malureanu R, Volkov VS, Bozhevolnyi SI, Lavrinenko AV. Direct characterization of plasmonic slot waveguides and nanocouplers. Nano Lett 2014;14:3925–9.
[47] Zenin VA, Malureanu R, Radko IP, Lavrinenko AV, Bozhevolnyi SI. Near-field characterization of bound plasmonic modes in metal strip waveguides. Optics Express 2016;24:4582–90.
[48] Zenin VA, Choudhury S, Saha S, Shalaev VM, Boltasseva A, Bozhevolnyi SI. Hybrid plasmonic waveguides formed by metal coating of dielectric ridges. Optics Express 2017;25:12295–302.
[49] Bogdanov SI, Boltasseva A, Shalaev VM. Overcoming quantum decoherence with plasmonics. Science 2019;364:532.
[50] Binder JM, Stark A, Tomek N. Qudi: a modular python suite for experiment control and data processing. SoftwareX 2017;6:85–90.
[51] Ocelic N, Huber A, Hillenbrand R. Pseudoheterodyne detection for background-free near-field spectroscopy. Appl Phys Lett 2006;89:101124.
[52] Johnson PB, Christy RW. Optical constants of the noble metals. Phys Rev B 1972;6:4370–9.
[53] Geisler P, Razinskas G, Krauss E, et al. Multimode plasmon excitation and in situ analysis in top-down fabricated nanocircuits. Phys Rev Lett 2013;111:183901.

Supplementary Material: The online version of this article offers supplementary material (https://doi.org/10.1515/nanoph-2020-0036).